IOE | Intelligent Opto-Electronics

Spectral-driven bidirectional design framework for polarization-selective structural colors

Tao Zhu, Ya Gao, Xi Chen, Xiaojin Chen, Jiao Geng, Liping Shi and Chenhui Lu

Citation: Zhu T, Gao Y, Chen X et al. Spectral-driven bidirectional design framework for polarization-selective structural colors. *Intelligent Opto-Electronics* **2**, 260012 (2026).

https://doi.org/10.67704/ioe.2026.260012

Received: 12 May 2026; Accepted: 29 July 2026; Published online: 15 September 2026

Related articles

OptoGPT: A foundation model for inverse design in optical multilayer thin film structures

Taigao Ma, Haozhu Wang, L. Jay Guo

Opto-Electronic Advances 2024, **7**(7): 240062 doi: 10.29026/oea.2024.240062

Modelling-guided inverse design strategy for semitransparent perovskite photovoltaics with customized colors

Seok-Beom Seo, Rira Kang, Eun-Joo Lee, et al

Opto-Electronic Advances 2026, **9**(2): 250218 doi: 10.29026/oea.2026.250218

More related articles in Opto-Electronic Journals Group website

Opto-Electronic Journals Group

OE_Journal

@OptoElectronAdv

IOE | Intelligent Opto-Electronics

Article

September 2026, Vol. 2, No. 3

Open Access

Spectral-driven bidirectional design framework for polarization-selective structural colors

Tao Zhu[1], Ya Gao[1]*, Xi Chen[2], Xiaojin Chen[2], Jiao Geng[3,4]*, Liping Shi[3,4] and Chenhui Lu[2]*

Abstract: The design of structural color metasurfaces typically relies on computationally expensive full-wave electromagnetic simulations and empirical parameter tuning, making it challenging to achieve efficient optimization in high-dimensional parameter spaces. We propose a forward-inverse neural network closed-loop framework for polarization-selective structural color design. In the forward modeling stage, a spectrally resolved multilayer perceptron is developed to explicitly learn the continuous mapping between structural parameters and reflection spectra, thereby enabling the joint optimization of spectral fidelity and perceptual color consistency. In the inverse design stage, a mixture density network (MDN) is introduced to model the multimodal distribution of structural parameters conditioned on a given target performance under different polarization conditions. The results demonstrate that the proposed method achieves excellent performance. After optimization, approximately 97% of the samples satisfy $\Delta E \leq 1$, with good spectral consistency maintained, thereby validating an effective balance between perceptual accuracy and physical fidelity. This work provides an efficient and reliable solution for the rapid inverse design of structural color, with potential applications in polarization-controlled displays and optical information encoding.

Keywords: structural color; inverse design; polarization-selective; spectral modeling

DOI: 10.67704/ioe.2026.260012

Citation: Zhu T, Gao Y, Chen X et al. Spectral-driven bidirectional design framework for polarization-selective structural colors. *Intell Opto-Electron* **2**, 260012 (2026).

1 Introduction

Structural colors based on subwavelength nanostructures[1–3] exhibit high saturation[4], excellent environmental stability, and long-term durability[5], making them highly promising for applications in color displays[6,7], optical anti-counterfeiting[8,9], and information encoding[10–12]. Unlike traditional color-generation mechanisms that rely on the absorption of pigments or dyes, structural color arises from the interaction between light and micro- and nanostructures[13–15], achieving selective modulation of the reflected spectrum through physical processes such as interference, diffraction, and resonant scattering[16,17]. Structural colors observed in butterfly wings and peacock feathers arise from wavelength-selective reflection of incident light by periodic micro- and nanostructures in nature. Inspired by these natural phenomena, artificially engineered metasurfaces[18–21] composed of designed nanostructures provide a highly flexible platform for precise control of structural color, enabling the realization of target spectra and colors through tailored geometric parameters.

At present, the design of structural color metasurfaces primarily relies on full-wave electromagnetic simulation methods, such as the finite element method (FEM) and the finite-difference time-domain (FDTD) method[22], often combined with parameter sweeps or heuristic optimization for structural exploration. However, in the presence of high-dimensional parameter spaces and complex parameter coupling, traditional simulation-based approaches relying on exhaustive search or empirical tuning typically require substantial computational resources, thereby limiting design efficiency—an issue that is particularly pronounced in structural color design. With the rapid development of machine

Received: 12 May 2026

Accepted: 29 July 2026

Published online: 15 September 2026

[1]School of Mathematics, Physics & Statistics, Shanghai University of Engineering Science, Shanghai 201620, China; [2]School of Mechanical and Automotive Engineering, Shanghai University of Engineering Science, Shanghai 201620, China; [3]Hangzhou Institute of Technology, Xidian University, Hangzhou 311231, China; [4]School of Optoelectronic Engineering, Xidian University, Xi'an 710071, Shaanxi, China.

*Correspondence: Y Gao, E-mail: gaoya@sues.edu.cn; J Geng, E-mail: gengjiao@xidian.edu.cn; CH Lu, E-mail: chlu@sues.edu.cn

learning techniques[23–26] in photonic device design[27–29] data-driven approaches[30–32] have emerged as an important means to accelerate metasurface design. By learning the mapping between structural parameters and optical responses, deep neural networks[33–36] can effectively replace a portion of computationally expensive full-wave simulations, enabling rapid prediction of spectral or color responses and thereby significantly improving design efficiency[37–39]. This provides a new technological pathway for both forward modeling and inverse design of structural color.

In recent years, deep learning-based inverse design approaches[40–43] for structural color have attracted widespread attention. In 2019, Gao et al.[44] proposed a neural network framework that enables efficient mapping between structural parameters and target colors, thereby significantly reducing the computational cost associated with conventional electromagnetic simulations. Subsequently, in 2024, Zuo et al.[45] employed a bidirectional long short-term memory (Bi-LSTM) network to realize polarization-insensitive inverse design of structural color, effectively improving both prediction accuracy and model generalization. Furthermore, in 2025, Yang et al.[46] proposed an LSTM-based cascaded network architecture that incorporates a feedback mechanism to partially alleviate the non-uniqueness inherent in inverse design, achieving high-accuracy structural color design. In contrast, the hybrid probabilistic sampling network proposed by Wei et al.[47] addresses the one-to-many mapping between optical performance and structural parameters in nanophotonic inverse design by sampling from a Gaussian mixture distribution and selecting optimal solutions.

Despite these advances in computational efficiency and prediction accuracy[48–50], most existing approaches formulate structural color design as a deterministic regression problem in a low-dimensional color space, directly establishing a mapping between structural parameters and RGB or chromaticity coordinates. This modeling approach overlooks the physical origin of structural color: the perceived color arises from the weighted integration of the reflection spectrum over the visible range, modulated by the illumination spectrum and the human visual response functions. Because different spectral distributions can correspond to the same perceived color, this many-to-one[51,52] mapping from "spectrum to color" inherently introduces information compression and irreversibility, leading to the prevalence of non-unique solutions in inverse design.

This issue becomes even more pronounced in polarization-dependent structural color design. For polarization-selective structures, the same nanostructure can exhibit markedly different spectral responses under different polarization states, while relying solely on color as the supervision signal is insufficient to constrain the consistency of the underlying electromagnetic response. This not only further exacerbates the ill-posed nature of the inverse mapping, but also leads to discrepancies in physical validation, thereby reducing the reliability and stability of the model.

To address the above issues, a hierarchical physical framework that incorporates spectroscopic information with physical completeness as an intermediate representation has emerged as a more reasonable modeling strategy. Compared with low-dimensional color representations, spectra provide a complete description of the structure's response across wavelengths, thereby offering stronger physical constraints for the model. Meanwhile, by explicitly constructing a hierarchical mapping of "structural parameters - reflection spectra - perceived color", the information collapse associated with direct color regression can be effectively avoided, thereby improving the physical consistency of inverse design results. First, a spectrum-prediction-driven forward model is constructed to achieve high-accuracy mapping from structural parameters to reflection spectra. Subsequently, in the inverse design stage, multimodal solution distribution modeling and a closed-loop optimization strategy are introduced to effectively characterize the multiple feasible solutions in the structural parameter space, while enforcing physical consistency through the forward model. This approach not only improves color matching accuracy, but also significantly enhances the stability and interpretability of inverse design, providing a new method for the efficient design of complex polarization-dependent structural colors.

2 Structure and design

AlN has been widely used in dielectric metasurfaces for optical manipulation, holography[53,54], and color engineering[55,56] due to its high refractive index and low light absorption. CeF_3 was selected as the substrate material because of its relatively low refractive index in the visible light range. Specifically, we obtained the refractive index of AlN from Pastrnák[57] and the refractive index of CeF_3 from Rodríguez-de Marcos[58]. These optical constants were used for all electromagnetic simulations.

In this work, the AlN metasurface consists of numerous unit cells. Figure 1(a) illustrates a schematic of the polarization-sensitive AlN nanostructure along with its geometric parameters. The metasurface is composed of periodically arranged AlN nanocolumns on a CeF_3 substrate. The geometric parameters of each unit include the nanocolumn length (L), width (W), height (H), and the period (P) between adjacent nanocolumns. Specifically, length (L) and width (W) range from 100 to 400 nm with a step size of 20, the period (P) varies from 250 to 410 nm with a step size of 10, and the nanocolumn height (H) is fixed at 325 nm.

Due to the in-plane geometric anisotropy of the nanocolumns, the structure exhibits distinctly different optical responses to different linearly polarized incident light under normal incidence. When the incident light is polarized along the x and y directions, respectively, the electromagnetic field distribution within the nanocolumn cross-section and its coupling with the structural boundaries

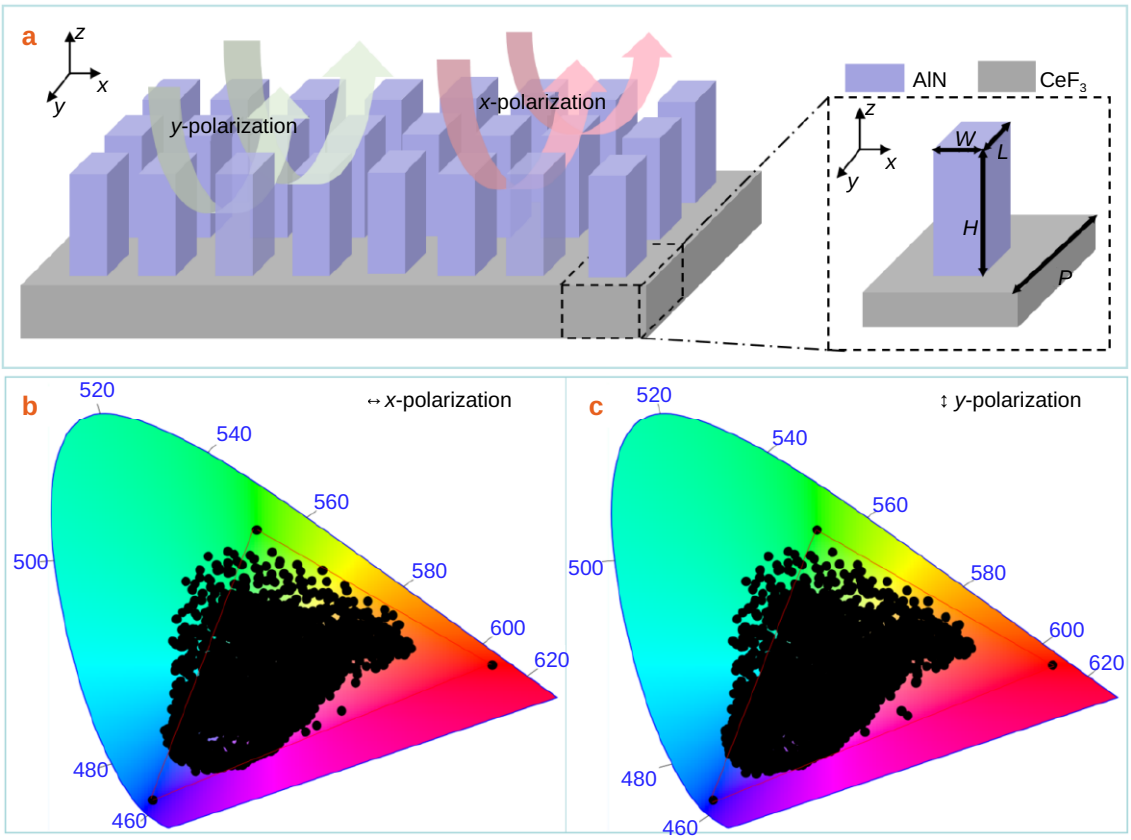

Fig. 1 | (a) Schematic of the investigated polarization-selective metasurface based on AlN nanostructures, along with the geometric parameters, including the nanocolumn length (L), width (W), height (H), and period (P). (b)–(c) Colors of the training dataset as displayed on the CIE 1931 color space chromaticity diagram, (b) *x*-polarization direction, and (c) *y*-polarization direction.

differ, thereby exciting distinct resonance modes. This polarization-dependent modal variation leads to significantly different reflection spectra and structural color responses under *x*- and *y*-polarized illumination, even for identical geometric parameters. To explicitly characterize this polarization-dependent behavior, full-wave electromagnetic simulations were performed for each set of geometric parameters under normal incidence with *x*- and *y*-polarized illumination, respectively. All simulations were carried out using COMSOL Multiphysics based on the finite element method (FEM), with a wavelength range of 400–700 nm. Other simulation conditions, including the incident angle and material properties, were kept consistent. In total, more than 2000 simulated spectra were generated for each polarization state. Therefore, the total number of simulated spectra across both polarization states exceeds 4000.

Within a unified colorimetric framework, the corresponding CIE tristimulus values X, Y, and Z of the reflection spectra are calculated as follows:

$$X = \frac{1}{K}\int_{\lambda} \bar{x}(\lambda)\, I(\lambda)\, S(\lambda)\, \mathrm{d}\lambda \,, \tag{1}$$

$$Y = \frac{1}{K}\int_{\lambda} \bar{y}(\lambda)\, I(\lambda)\, S(\lambda)\, \mathrm{d}\lambda \,, \tag{2}$$

$$Z = \frac{1}{K}\int_{\lambda} \bar{z}(\lambda)\, I(\lambda)\, S(\lambda)\, \mathrm{d}\lambda \,, \tag{3}$$

here, I(λ) denotes the relative spectral power distribution of the incident light; S(λ) represents the reflection spectrum obtained via the finite element method, and $\bar{x}(\lambda)$, $\bar{y}(\lambda)$ and $\bar{z}(\lambda)$ are the standard observer color matching functions defined by the International Commission on Illumination. K is a normalization constant. The chromaticity coordinates are then calculated from the tristimulus values as follows:

$$x = \frac{X}{X+Y+Z} \,, \tag{4}$$

$$y = \frac{Y}{X+Y+Z} \,. \tag{5}$$

The calculated chromaticity coordinates are plotted on the CIE-1931 XYZ chromaticity diagram, yielding the datasets under *x*- and *y*-polarized conditions, as shown in Fig. 1(b) and 1(c), respectively. Meanwhile, to quantitatively evaluate the discrepancy between the predicted and ground-truth colors, the color difference was evaluated using the CIEDE2000 metric (ΔE), which provides a perceptually relevant measure of color discrepancy.

Furthermore, to facilitate comparison of structural color variations induced by spectral differences under different polarization conditions, the colors computed from the reflection spectra are subjected to a unified luminance normalization, with the luminance component Y fixed at 0.5. This ensures that the visualization primarily reflects variations in spectral shape rather than differences in absolute reflectance intensity. Representative reflection spectra under *x*- and *y*-polarized illumination for selected structural parameters are compared in Fig. 2(a–d). It can be observed that the reflection spectra corresponding to different linearly polarized incidences exhibit significant differences in resonance peak positions, peak intensities, and spectral profiles under identical geometric parameters. This polarization-dependent spectral response originates from the anisotropic geometry of the nanocolumns, which leads to distinct electromagnetic mode coupling. The resonance modes excited under different polarization states differ markedly in their spatial field distributions and resonance conditions, thereby resulting in pronounced variations in the reflection spectra.

3 Forward prediction network

To avoid the information collapse associated with directly regressing chromaticity coordinates in a low-dimensional color space, a spectrally resolved forward prediction model is constructed, as shown in Fig. 3(a), to explicitly learn the continuous mapping between the geometric parameters of the nanostructure and its wavelength-dependent reflection spectra. This strategy preserves the complete spectral information in the mapping from structural parameters to perceived color, allowing the network to fully capture the continuous variations of the optical response and thereby providing a physically grounded basis for subsequent inverse design. In this work, the *x*-polarization and *y*-polarization reflection spectra were simulated independently for the same structural parameter space, resulting in two polarization-specific datasets. Accordingly, two independent forward prediction models with identical network architectures were trained separately for the *x*- and *y*-polarized cases. On this basis, a multilayer perceptron is employed as

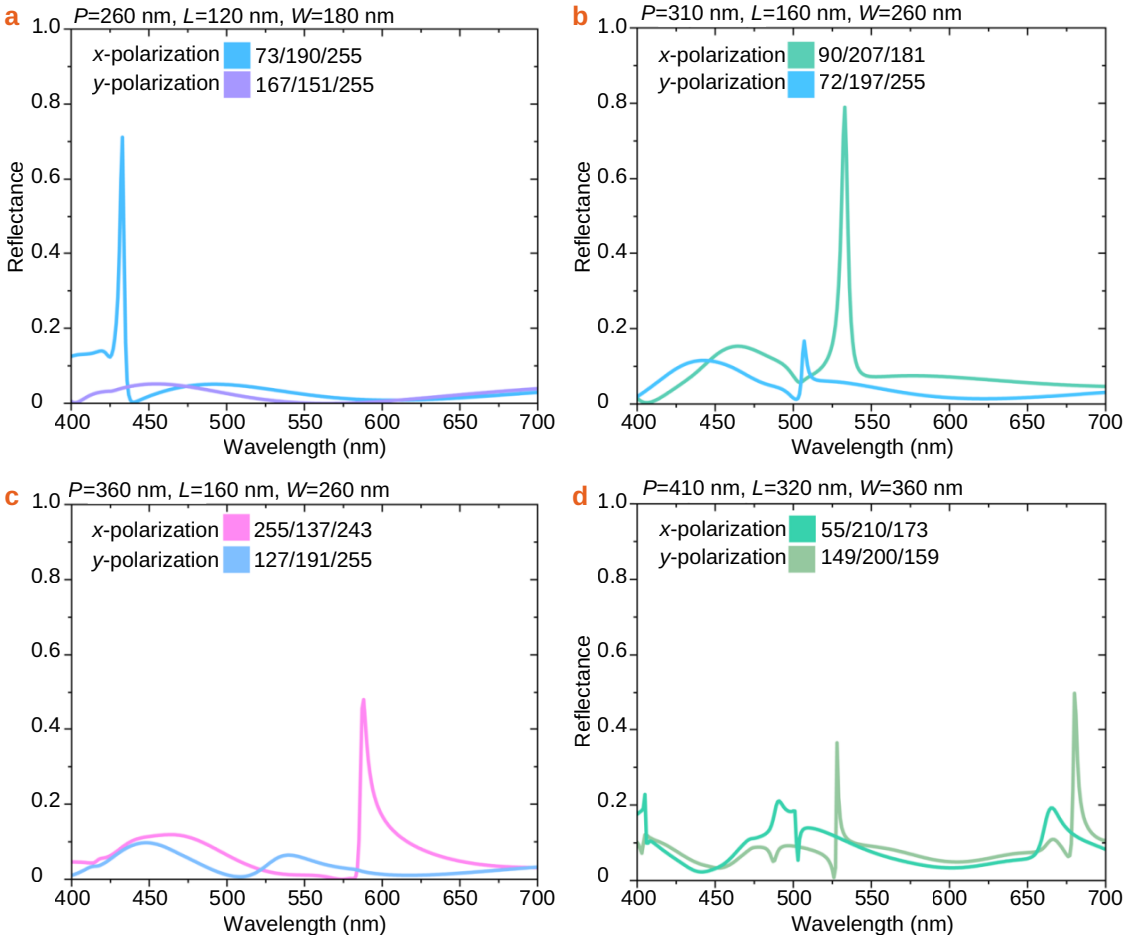

Fig. 2 | (a)–(d) Comparison of reflection spectra for several sets of nanostructural parameters under normal incidence with *x*- and *y*-polarized illumination. The structural colors are visualized based on the calculated reflection spectra, with the luminance component (Y) uniformly normalized to 0.5.

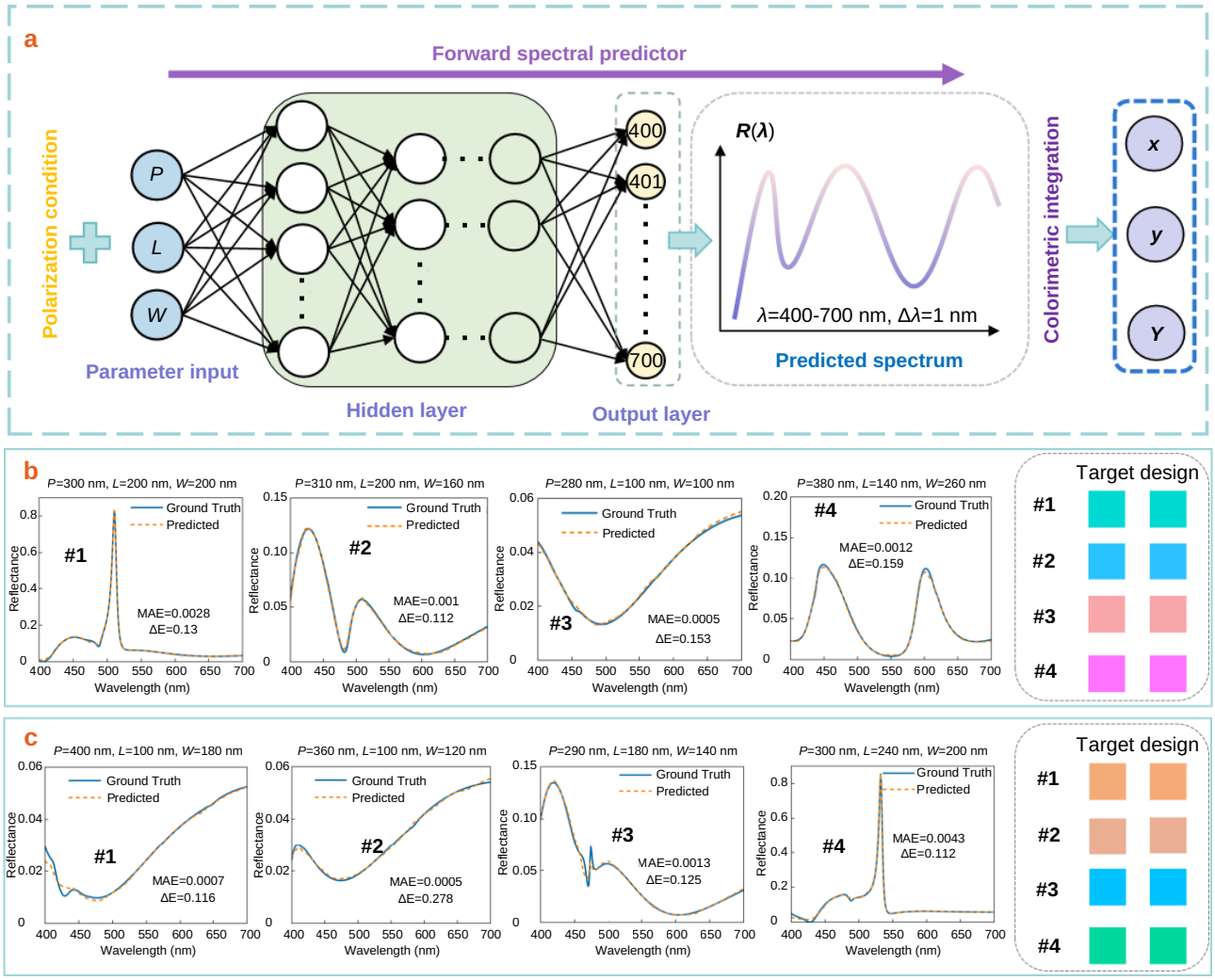

Fig. 3 | (a) Schematic diagram of the model structure, with structural parameters as inputs under different polarization conditions, and reflection spectra in the 400–700 nm range as outputs, which are further converted to a color space. (b) Spectral prediction results for a typical sample under *x*-polarization; the blue line represents the actual values, and the orange line represents the predicted values. (c) Spectral prediction results for a typical sample under *y*-polarization; the blue line represents the actual values, and the orange line represents the predicted values.

the forward model to learn the nonlinear mapping between structural geometric parameters and the reflection spectra. For different polarization conditions, separate datasets are constructed and independent forward prediction models are trained accordingly. For each model, the inputs consist of the structural geometric parameters, while the output is the corresponding reflection spectrum under the given polarization condition. The entire dataset is divided into training, validation, and test sets with proportions of 75%, 15%, and 10%, respectively.

The feedforward network consists of multiple layers of fully connected neurons, with each hidden layer using the ReLU activation function to enhance its nonlinear representational capacity. The output layer is first compressed using the Tanh activation function, then undergoes a linear transformation and clipping operation to restrict the predicted reflectance to the physically plausible range of [0,1]. This network architecture balances expressive power with training stability and compliance with physical constraints. During training, the Adam optimizer is used to update the model parameters, and a cosine-smoothed learning rate scheduling strategy is employed to dynamically adjust the learning rate, thereby accelerating convergence and preventing the model from getting stuck in local optima. An early stopping mechanism is implemented during training to prevent overfitting.

Given that spectral amplitude accuracy, spectral shape, and physical feasibility all significantly influence perceived color in structural color design, this paper proposes a multi-constraint composite loss function that jointly constrains the predicted spectrum across multiple complementary dimensions. The mean squared error (MSE) serves as the

dominant term, constraining wavelength-specific amplitude errors; the cosine similarity (CosineLoss) constrains spectral shape; the SmoothLoss term acts on the first-order difference of the spectrum to suppress non-physical oscillations and encourage smooth spectral transitions; and GradMatch preserves peak positions and slope characteristics. Specifically, the spectral loss is defined as follows:

$$\mathcal{L}_1 = \alpha\mathcal{L}_{\mathrm{MSE}} + \beta\mathcal{L}_{\mathrm{CosineLoss}} + \gamma\mathcal{L}_{\mathrm{SmoothLoss}} + \delta\mathcal{L}_{\mathrm{GradMatch}} . \quad (6)$$

In this model, α= 0.7, β= 0.2, γ= 0.05, and δ= 0.05 are the weighting coefficients. To improve perceived color consistency, the predicted spectrum is converted to chromaticity coordinates using the CIE color matching function, and the error is calculated relative to the target chromaticity to construct the color loss term:

$$\mathcal{L}_2 = \mathcal{L}_{\mathrm{xy}} + \lambda_{\mathrm{Y}}\mathcal{L}_{\mathrm{Y}} , \quad (7)$$

here, $\mathcal{L}_{\mathrm{xy}}$ is used to constrain the chromaticity coordinates (x, y), and $\mathcal{L}_{\mathrm{Y}}$ is used to constrain the luminance component Y. λ_c serves as the weight coefficient for the color loss term in the total loss function. The final total loss function $\mathcal{L}$ is defined as:

$$\mathcal{L} = \mathcal{L}_1 + \lambda_c\mathcal{L}_2 . \quad (8)$$

The model was trained for 1,000 epochs (epoch = 1,000) with a batch size of 32 (BatchSize = 32), and an early stopping mechanism was implemented to prevent overfitting. The training loss is shown in Fig. 4(a) and 4(c). Under various polarization conditions, we systematically evaluated the predictive performance of the proposed MLP forward model for the reflectance spectra of micro- and nanostructures and their corresponding structural colors. The model uses structural parameters as input to directly predict reflectance spectra in the 400–700 nm wavelength range and further calculates structural color and color difference indices using standard colorimetric integrals. Figure 3(b) and 3(c) show several representative samples, comparing the actual and predicted spectra, as well as the target and design colors, under different polarization conditions. These samples exhibit distinct spectral profiles. It can be observed that the model is capable of accurately reconstructing the positions of major resonance peaks and the overall spectral shape. Particularly within the resonance bands responsible for the dominant structural colors, the predicted results show a high degree of consistency with numerical simulations. This indicates that, under ideal conditions, the proposed forward model not only achieves high-fidelity spectral predictions but also accurately reproduces structural color characteristics at the perceptual level.

To further analyze the model's predictive performance across different wavelength bands, Figure 4(e) shows the mean absolute error (MAE) of reflectance predictions on the test set as a function of wavelength. As can be seen, the overall MAE ranges from approximately 0.005 to 0.01, corresponding to an absolute error of less than 1% within the reflectance range [0,1]. Furthermore, as shown in Fig. 4(b) and 4(d), over 95% of the structural colors predicted from the spectra under different polarization conditions, as obtained through chromaticity integration, meet the perceptual threshold of ΔE ≤ 3. It should be noted that structural colors are dominated by narrow-band spectral resonances, and their color perception is highly sensitive to the position

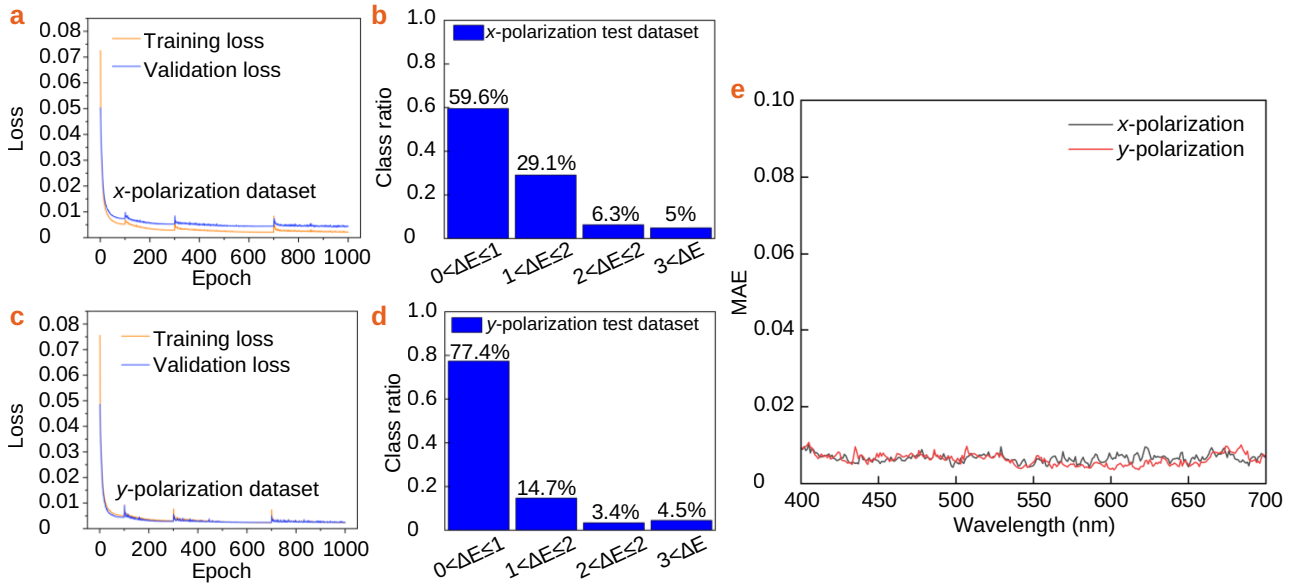

Fig. 4 | (a) and (c) Training and validation losses under *x*-polarization and *y*-polarization. (b) and (d) Statistical distributions of the color difference between predicted and target colors for *x*-polarization and *y*-polarization directions. (e) Distribution of spectral prediction errors under different polarization conditions.

of these resonance peaks. Since the chromaticity integration process introduces non-uniform weighting between the human eye's sensitivity function and the light source spectrum, even resonance peak shifts on the order of a few nanometers can cause significant changes in the CIE color space. Furthermore, color difference metrics exhibit a nonlinear amplification effect for hue changes; this amplification effect is particularly pronounced near high saturation or at the boundaries of the color gamut.

4 Inverse design network

The forward mapping process from structure to color essentially involves a projection from a high-dimensional spectral space into a low-dimensional perceptual space. Specifically, structural parameters first determine their wavelength-dependent reflectance spectra, which are then mapped to a low-dimensional color perceptual space through chromaticity integration. This mapping process from spectral to chromaticity inevitably introduces irreversible information compression, resulting in different combinations of structural parameters potentially producing nearly identical color responses in perceptual terms. Precisely because of the irreversibility introduced by the spectral-to-color-perception integration process, the forward mapping from structural parameters to chromatic responses exhibits distinct non-injective characteristics. In the parameter space, such structurally distinct but perceptually indistinguishable solutions are not discretely distributed; rather, they form a set of structural parameters that are equivalent within the range of perceptual tolerance.

Traditional inverse design methods often overlook the inherent multi-solution nature of the problem. In contrast, this study aims to characterize the distribution of solutions by introducing a mixture density network (MDN) to model the multimodal conditional probability distribution of structural parameters under perceptual constraints, thereby systematically describing the various geometric solutions that may exist under perceptual consistency constraints. The inverse-engineering framework is shown in Fig. 5. In this work, the inverse design is performed in a polarization-conditioned manner. Specifically, for a specified incident polarization state, the desired color or reflection spectrum is used as the target input, and the inverse model predicts candidate structural parameters that can reproduce the target optical response under that polarization condition.

Since the output results are not single, deterministic values for structural parameters, the network architecture primarily consists of a set of feedforward neural networks, with a parametric Gaussian mixture model (GMM) cascaded

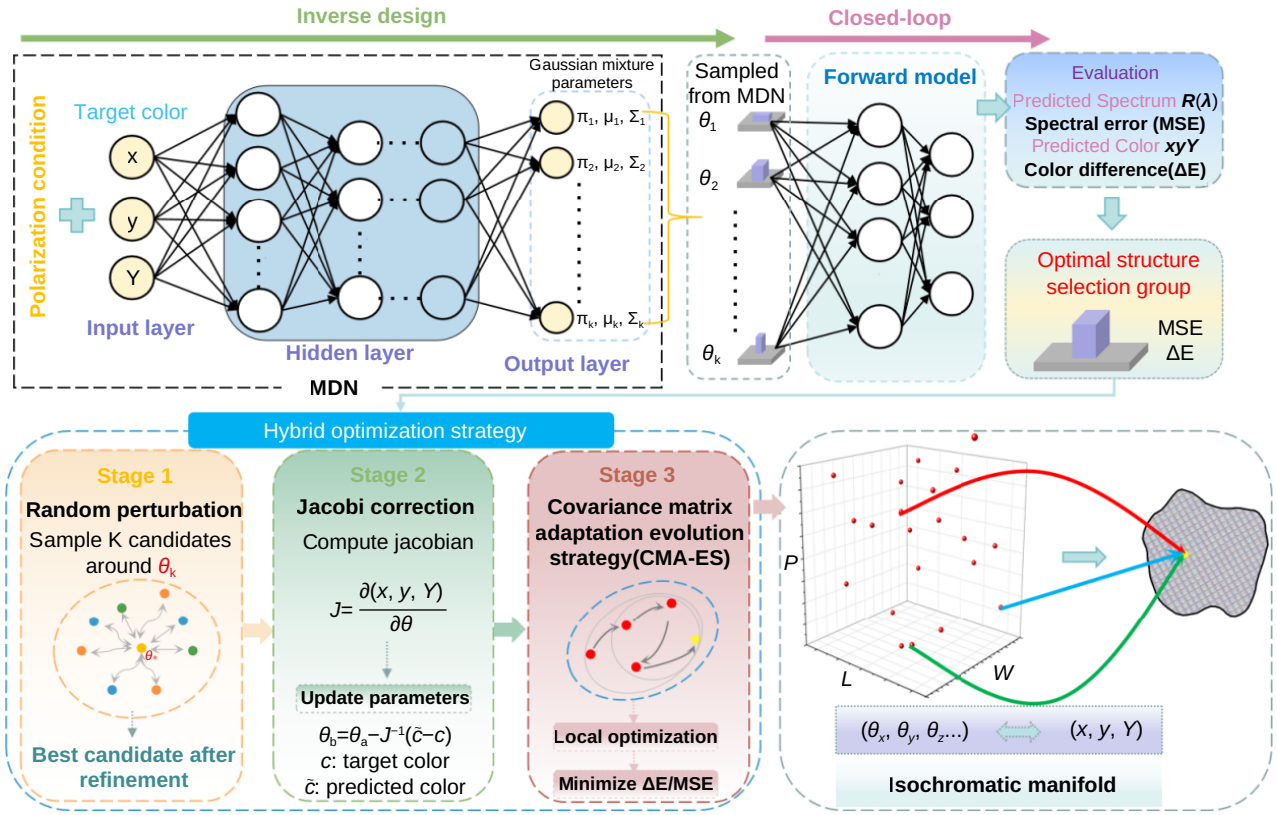

Fig. 5 | Schematic diagram of a framework for the inverse design of structural color based on a mixture density network and a hybrid optimization strategy.

at the end of the network. The Gaussian mixture distribution replaces deterministic regression values to describe the multimodal characteristics of structural parameters. The backbone network consists of multiple hidden layers and uses ReLU as the activation function. The Adam optimizer is employed with a learning rate of 0.001, and a weight decay term ($\lambda = 0.00001$) is introduced to suppress overfitting. The fully connected output layer of a mixture density network does not directly predict geometric parameters; instead, it outputs all parameters required for the Gaussian mixture model, including mixing weights and mean vectors. Since traditional loss metrics commonly used in regression tasks, such as MSE, cannot capture the multi-solution structure, it is difficult to drive the network to learn multiple possible structural clusters. To ensure that the predicted distribution approximates the statistical distribution of the parameters as closely as possible, the inverse model loss function employs negative log-likelihood (NLL) as the training loss. The probability distribution and the negative log-likelihood are expressed as follows:

$$\mathrm{p}\left(\boldsymbol{p}|\mathrm{c}\right) = \sum_{\mathrm{k}=1}^{\mathrm{K}} \pi_{\mathrm{k}} \mathcal{N}\left(\boldsymbol{p}|\boldsymbol{\mu}_{\mathrm{k}}, \Sigma_{\mathrm{k}}\right), \tag{9}$$

$$\mathcal{L}_{\mathrm{MDN}} = -\log\left(\sum_{\mathrm{k}=1}^{\mathrm{K}} \pi_{\mathrm{k}} \mathcal{N}\left(\boldsymbol{p} \mid \boldsymbol{\mu}_{\mathrm{k}}, \sum_{\mathrm{k}}\right)\right). \tag{10}$$

Here, given chromaticity c = (x, y, Y), $\boldsymbol{p}$ represents the structural parameters; K denotes the number of Gaussian components in the mixture distribution (the number of mixtures); π_{k} represents the corresponding probability weight; μ_{k} denotes the latent candidate solution; Σ_{k} describes the uncertainty of this structural solution; and $\mathcal{N}$ is the probability density. In the network, the mean μ_{k} of each Gaussian component forms a complete vector of structural parameters. These component means μ_{k}, taken as a whole, constitute the initial candidate solution for inverse design.

Although mixture density network can statistically characterize the multi-solution nature of inverse mapping, the chromatic responses of their directly generated candidate solutions in real physical models may still deviate from the target. Notably, given that the inverse mapping from structural parameters to perceptual color is highly nonlinear and inherently multi-solution, relying solely on the direct output of GMMs makes it difficult to ensure the reliability of candidate solutions in terms of perceptual color consistency and engineering feasibility. Based on this, this paper further introduces a hybrid compensation optimization strategy on top of probabilistic inverse modeling. By forming a closed-loop system between the statistically generated candidate structural parameters and the forward physical model, we perform constrained optimization of perceptual errors within the chromatic manifold neighborhood, thereby bridging the gap between probabilistic modeling and physical consistency.

Specifically, the inverse model first generates multiple sets of candidate structural parameter solutions under perceptual constraints, and then uses a forward surrogate model to explicitly calculate the perceptual color difference between the predicted and target chromaticity values, thereby completing the initial screening and ranking. Building on this, a three-stage hybrid optimization strategy is applied to refine the top-ranked candidate solutions: (i) Stochastic local optimization introduces controlled perturbations within the neighborhood of the candidate solutions to enhance search diversity and reduce the risk of getting stuck at local optima; (ii) Linear compensation based on the Jacobian matrix utilizes local sensitivity information from the forward model to apply corrections with clear physical significance to the structural parameters, thereby effectively reducing perceptual color difference in a first-order approximation; (iii) An evolutionary search strategy further performs constrained exploration in the nonlinear optimization process, yielding structural parameter solutions with smaller color differences in terms of perceptual consistency. It should be emphasized that this hybrid optimization process uses the continuous reduction of perceptual chromatic aberration ΔE as its primary criterion, implicitly implementing constrained search within the isochromatic manifold neighborhood in the parameter space through an inverse-forward closed-loop verification.

Figure 6(a) and 6(b) present the statistical results of color difference distributions under different polarization conditions. Without optimization, the structural parameters generated by the inverse model exhibit a relatively dispersed distribution in terms of perceptual accuracy. Under *x*-polarization conditions, only 30.9% of the samples met the high-precision requirement of $\Delta E \leq 1$, with the majority of samples concentrated in the $1 \leq \Delta E \leq 2$ range (39.7%), while approximately 14% of the samples still had errors exceeding $\Delta E > 3$. A similar trend is observed under *y*-polarization conditions, with 36.6% of samples meeting the $\Delta E \leq 1$ criterion, but the overall error distribution remains relatively dispersed. This indicates that although the mixture density network can capture the multi-solution distribution in a statistical sense, the candidate structures it directly outputs still exhibit some deviation in terms of perceptual consistency.

In contrast, after introducing the proposed hybrid compensation optimization strategy, the error distribution converged significantly. Under the two polarization conditions, the proportion of cases where $\Delta E \leq 1$ increased to 96.9% and 97.3%, respectively. These results demonstrate that through a closed-loop optimization process involving a forward model, perceived chromatic aberration can be effectively utilized as a feedback signal to guide candidate structures toward the optimal solution within the isochromatic manifold neighborhood in parameter space, thereby significantly improving the accuracy and stability of the

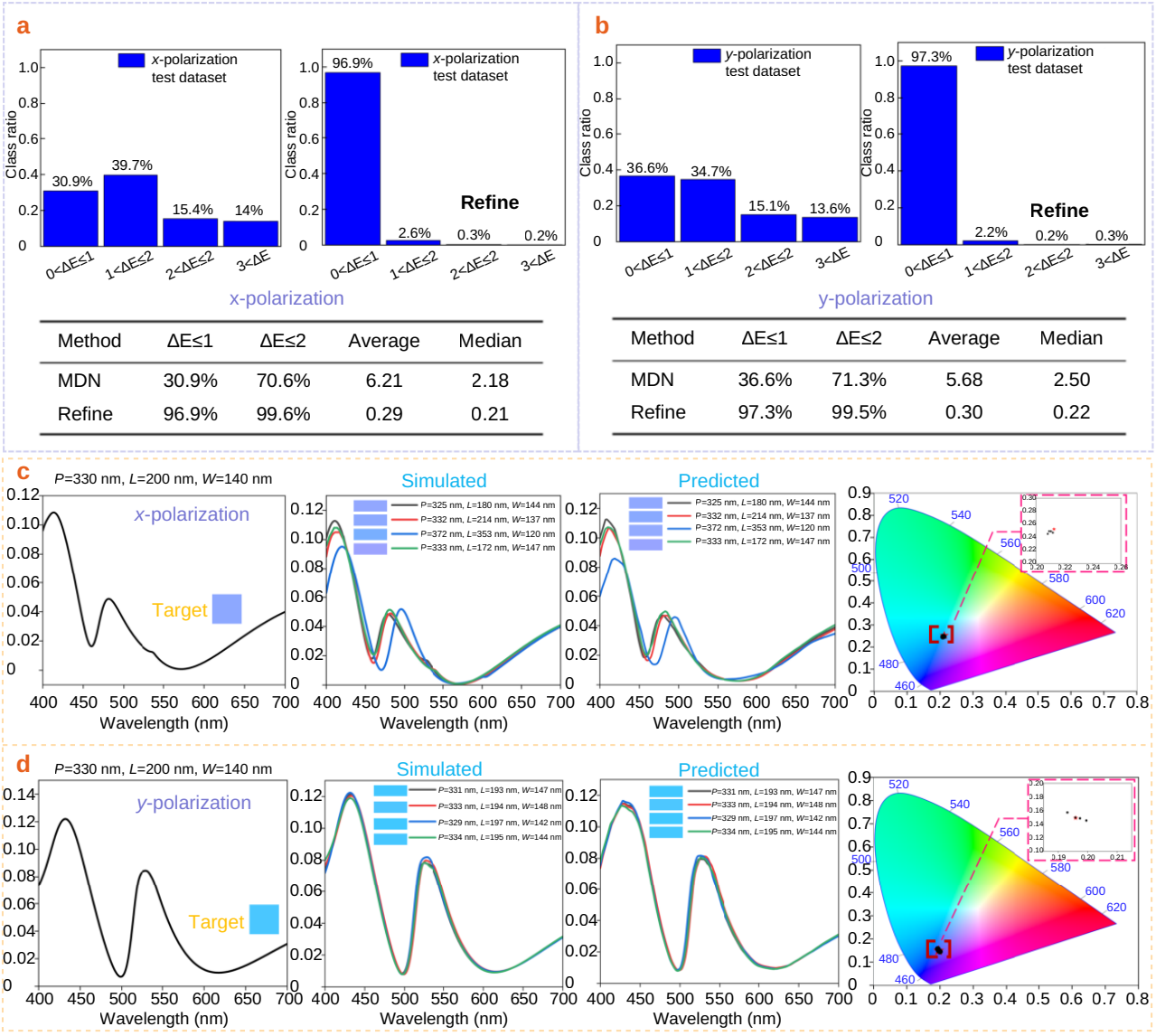

Method	ΔE≤1	ΔE≤2	Average	Median
MDN	30.9%	70.6%	6.21	2.18
Refine	96.9%	99.6%	0.29	0.21

Method	ΔE≤1	ΔE≤2	Average	Median
MDN	36.6%	71.3%	5.68	2.50
Refine	97.3%	99.5%	0.30	0.22

Fig. 6 | (a) Color difference (ΔE) distribution and statistical results before and after optimization under *x*-polarization. (b) Color difference (ΔE) distribution and statistical results before and after optimization under *y*-polarization conditions. (c) Inverse design of the parameter set *P* = 330 nm, *L* = 200 nm, *W* = 140 nm under *x*-polarization. (d) Inverse design of the parameter set *P* = 330 nm, *L* = 200 nm, *W* = 140 nm under *y*-polarization.

inverse design.

To demonstrate the multi-solution capability of the inverse design, Figure 6(c) and 6(d) show a comparison of inverse designs under different polarization conditions for the parameter set (*P* = 330 nm, *L*= 200 nm, *W*= 140 nm). Further comparison of the results under different polarization conditions reveals that the proposed method exhibits consistent spectral trends under both *x*-polarization and *y*-polarization, indicating that this framework addresses the multi-solution problem in structural color design. Overall, through a closed-loop mechanism of "statistical modeling —physical validation —iterative compensation", this hybrid compensation optimization framework expands inverse design from convergence to a single solution to a systematic exploration of isochromatic manifolds, thereby achieving a balance between perceptual consistency, physical plausibility, and engineering feasibility.

It should be noted that our model possesses polarization-generalization capabilities and can be extended to non-polarized opto-electronic devices, since the core structure–spectrum relationship is governed by the same Maxwell equations and constrained by the same low-dimensional geometric parameter space. However, in our present framework, the specified polarization state is used as an input variable since our work focuses on the specific structure–spectrum relationship under a given polarization

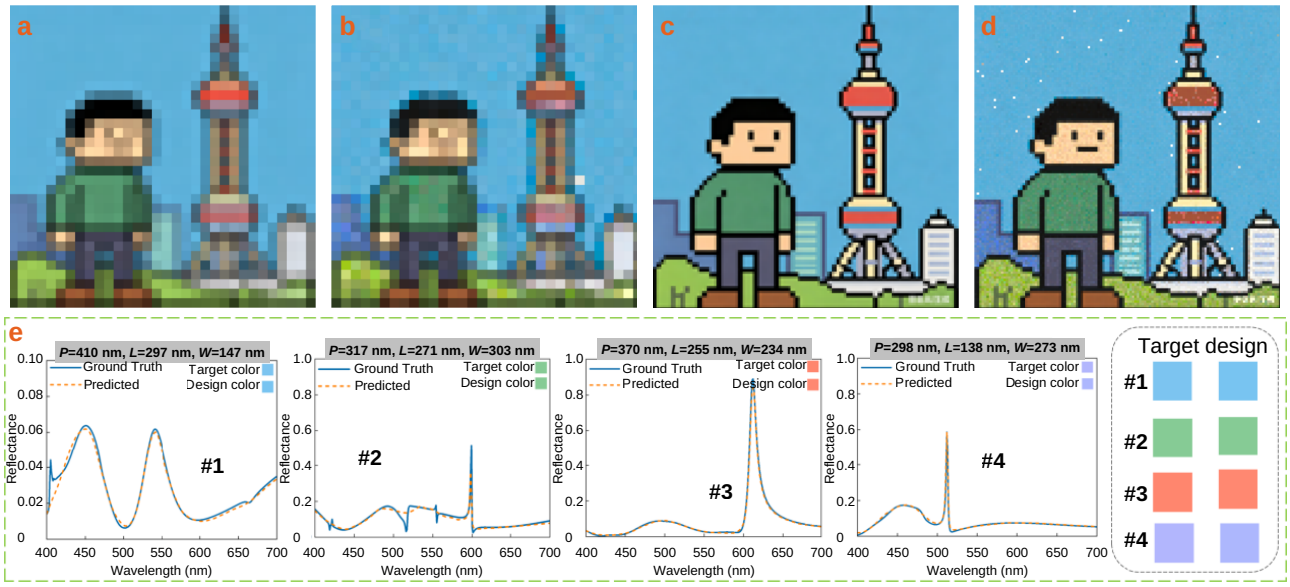

Fig. 7 | (a) Target image at 32×32 pixels. (b) Inverse design image at 32×32 pixels under *x*-polarization. (c) Target image at 128×128 pixels. (d) Inverse design image at 128×128 pixels.(e) Representative pixel spectra comparison under *x*-polarization.

condition and its corresponding structural color response and reveals the underlying physical mechanisms, which provides important insights for the research and design of polarization-based opto-electronic devices.

Finally, we extracted pixels from the same image at different resolutions and fed them into the inverse model. The reconstruction process was performed under *x*-polarization. Specifically, Figure 7(a) and 7(b) show the target image and the inversely reconstructed image at 32×32 pixels, respectively. It can be observed that the model effectively restores the overall color distribution and spatial structural features of the target image; however, due to the limited number of pixels at low resolutions, the reconstructed results exhibit some degree of pixelation. Furthermore, Figure 7(c) and 7(d) show the target image and the reconstructed result at 128×128 pixels, respectively. For each selected pixel, we provide the spectrum predicted by the network model and the full-wave simulated spectrum. The comparison between the predicted spectrum and the full-wave simulated spectrum shows good consistency, indicating that the reconstructed color is physically supported by the designed nanostructure. Compared to the low-resolution case, high-resolution reconstruction further enhances image detail and visual continuity. The overall results demonstrate that the proposed MDN multi-solution inverse design framework can effectively reconstruct complex spatial color distributions while maintaining good overall color consistency across different resolutions.

In addition, the designed unit cells have regular and well-defined geometries, with lateral dimensions and periods in the range of hundreds of nanometers, avoiding extremely small features that are difficult to fabricate. Therefore, they are compatible with standard nanofabrication processes such as electron-beam lithography, nanoimprint lithography, and dry etching. In terms of fabrication tolerance, the generated structural colors are mainly determined by the overall reflection spectra in the visible range rather than by a single ultra-narrow resonance. Thus, moderate geometrical deviations are expected to cause only limited spectral shifts or intensity variations. Moreover, the continuous parameter space and the non-unique nature of structural color inverse design provide the possibility of selecting candidate structures with better fabrication accessibility and tolerance.

5 Conclusion

In this work, we have developed an efficient inverse design method for polarization-selective structural color. By constructing a modeling framework based on spectral information and combining multi-solution distribution learning with a closed-loop optimization mechanism, we have effectively described and controlled the complex mapping relationship between structural parameters and perceived color. Furthermore, the multi-solution nature of the model provides additional design freedom for structural color design. Under identical color response conditions, different structural parameter schemes can be selected based on specific requirements, thereby enhancing design flexibility and feasibility. This expansion of the design space, driven by "multi-solution" capabilities, endows the method with greater adaptability for practical engineering applications.

Overall, the proposed method achieves high-precision and high-efficiency structural color inverse engineering while ensuring physical consistency. It also offers an effective approach for addressing the issue of non-uniqueness in complex photonic structures and has the potential to be

extended to a wider range of nanophotonic device design tasks.

References

1. Liu MZ, Zhu WQ, Huo PC et al. Multifunctional metasurfaces enabled by simultaneous and independent control of phase and amplitude for orthogonal polarization states. *Light Sci Appl* **10**, 107 (2021).
2. Yang WH, Xiao SM, Song QH et al. All-dielectric metasurface for high-performance structural color. *Nat Commun* **11**, 1864 (2020).
3. Wang JJ, Lu CH, Geng J et al. Polarization-switchable structural colors generated by AlN metasurfaces and the effect of different substrates. *AIP Adv* **14**, 105209 (2024).
4. Yang B, Liu WW, Li ZC et al. Ultrahighly saturated structural colors enhanced by multipolar-modulated metasurfaces. *Nano Lett* **19**, 4221–4228 (2019).
5. Li YJ, Hu JT, Zeng YX et al. Recent progress on structural coloration. *Photonics Insights* **3**, R03 (2024).
6. Wang F, Czarske JW, Situ G. Deep learning for computational imaging: from data-driven to physics-enhanced approaches. *Adv Photonics* **7**, 054002 (2025).
7. Liang SY, Liu YF, Ji ZK et al. High-resolution full-color quantum dots patterning for display applications based on femtosecond laser-induced forward transfer. *Laser Photonics Rev* **18**, 2300388 (2024).
8. Yuan H, Zhong ZQ, Zhang B. Neural network assisted end-to-end design for broadband high diffraction efficiency full-color meta-holograms. *Laser Photonics Rev* **19**, e00946 (2025).
9. Park C, Jeon Y, Rho J. 36-channel spin and wavelength Co-multiplexed metasurface holography by phase-gradient inverse design. *Adv Sci* **12**, 2504634 (2025).
10. Song MW, Feng L, Huo PC et al. Versatile full-colour nanopainting enabled by a pixelated plasmonic metasurface. *Nat Nanotechnol* **18**, 71–78 (2023).
11. Jiang HM, Li ZG, Zhang DS. Femtosecond laser maskless direct writing of dual-band crosstalk-free information for all-in-one high-security encryption metasurface. *Opto-Electron Adv* **9**, 250303 (2026).
12. Ren YZ, Jin RC, Song MW et al. High-performance color printing and information encryption enabled by silicon carbide metasurface. *Adv Funct Mater* **36**, e26191 (2026).
13. Xu T, Shi HF, Wu YK et al. Structural colors: from plasmonic to carbon nanostructures. *Small* **7**, 3128–3136 (2011).
14. Zhang N, Gao F, Wang RD et al. Deep-learning empowered customized chiral metasurface for calibration-free biosensing. *Adv Mater* **37**, 2411490 (2025).
15. Madeleine T, Podoliak N, Buchnev O et al. Topological learning for the classification of disorder: an application to the design of metasurfaces. *ACS Nano* **18**, 630–640 (2024).
16. Fan QB, Xu WZ, Hu XM et al. Disordered metasurface enabled single-shot full-Stokes polarization imaging leveraging weak dichroism. *Nat Commun* **14**, 7180 (2023).
17. Li YJ, Yin J, Zhang C et al. All-dielectric Schrödinger colours across the visible spectrum. *Nat Commun* **17**, 275 (2026).
18. Pearson P, Roberts G, Faraon A. Inverse-designed metasurfaces for multifunctional spatial frequency filtering. *Optica* **12**, 1090–1099 (2025).
19. Ma W, Liu ZC, Kudyshev ZA et al. Deep learning for the design of photonic structures. *Nat Photonics* **15**, 77–90 (2021).
20. Yeung C, Tsai R, Pham B et al. Global inverse design across multiple photonic structure classes using generative deep learning. *Adv Opt Mater* **9**, 2100548 (2021).
21. Chen MK, Lupoiu R, Mao CK et al. High speed simulation and freeform optimization of nanophotonic devices with physics-augmented deep learning. *ACS Photonics* **9**, 3110–3123 (2022).
22. Yu XS, Chen X, Cheng XJ et al. Polarization-selective terahertz absorber based on square cyclic graphene surface. *Mater Today Commun* **41**, 110268 (2024).
23. Wu NF, Sun YX, Hu JT et al. Intelligent nanophotonics: when machine learning sheds light. *eLight* **5**, 5 (2025).
24. Xu YJ, Liu X, Cao X et al. Artificial intelligence: a powerful paradigm for scientific research. *Innovation* **2**, 100179 (2021).
25. Si LM, Niu R, Dang CY et al. Advances in artificial intelligence for artificial metamaterials. *APL Mater* **12**, 120602 (2024).
26. Zandehshahvar M, Kiarashi Y, Zhu ML et al. Metric learning: harnessing the power of machine learning in nanophotonics. *ACS Photonics* **10**, 900–909 (2023).
27. Lupoiu R, Shao YX, Dai TX et al. A multi-agentic framework for real-time, autonomous freeform metasurface design. *Sci Adv* **11**, eadx8006 (2025).
28. Gong CJ, Shi HD, Wang Q et al. Design and optimization of full-stokes hyperspectro-polarimetric encoding metasurfaces based on conditional multi-task deep learning. *Adv Sci* **13**, e23143 (2026).
29. Fang R, Ghasemi A, Zeze D et al. Inverse design of lateral hybrid metasurfaces structural colour: an AI approach. *RSC Adv* **14**, 25678–25684 (2024).
30. Barati Sedeh H, George RC, Lai FX et al. Toward the meta-atom library: experimental validation of machine learning-based Mietronics. *Adv Photonics* **7**, 036004 (2025).
31. An SS, Fowler C, Zheng BW et al. A deep learning approach for objective-driven all-dielectric metasurface design. *ACS Photonics* **6**, 3196–3207 (2019).
32. Li XZ, Shu J, Gu WH et al. Deep neural network for plasmonic sensor modeling. *Opt Mater Express* **9**, 3857–3862 (2019).
33. Shan SC, Ye H, Yang ZM et al. Color2Struct: efficient and accurate deep-learning inverse design of structural color with controllable inference. *Opt Express* **34**, 13123–13132 (2026).
34. Wang JH, Lin ZC, Fan Y et al. Design of all-dielectric metasurface-based subtractive color filter by artificial neural network. *Materials* **15**, 7008 (2022).
35. Yang R, Chen L, Wang Z et al. Metasurface-based wavelength-multiplexed diffractive neural networks for multilabel intelligent vision. *Nano Lett* **26**, 5825–5832 (2026).
36. Cao ZY, Du HJ, Yuan XJ et al. Programmable three-dimensional photonic neural network chip. *Nat Commun* **17**, 5476 (2026).
37. Ma TG, Wang HZ, Guo LJ. OptoGPT: a foundation model for inverse design in optical multilayer thin film structures. *Opto-Electron Adv* **7**, 240062 (2024).
38. Gu Z, Ma Q, Han ZQ et al. Space-time holograms based on programmable metasurfaces. *Nat Electron* **9**, 919–931 (2026).
39. Ding ZP, Su W, Luo YL et al. Metasurface inverse designed by deep learning for quasi-entire terahertz wave absorption. *Nanoscale* **16**, 1384–1393 (2024).
40. Liu C, Zhang JL, Zhao YP et al. Inverse design of plasmonic nanohole arrays by combing spectra and structural color in deep learning. *Adv Intell Syst* **5**, 2300121 (2023).
41. Kim MJ, Kim JT, Hong MJ et al. Deep learning-assisted inverse design of nanoparticle-embedded radiative coolers. *Opt Express* **32**, 16235–16247 (2024).
42. Choi M, Xiang JL, Wirth-Singh A et al. Transferable polychromatic optical encoder for neural networks. *Nat Commun* **16**, 5623 (2025).
43. Tahersima MH, Kojima K, Koike-Akino T et al. Deep neural network inverse design of integrated photonic power splitters. *Sci Rep* **9**, 1368 (2019).
44. Gao L, Li XZ, Liu DJ et al. A bidirectional deep neural network for accurate silicon color design. *Adv Mater* **31**, 1905467 (2019).
45. Zuo Y, Ni B, Zhou YR et al. Inverse design of polarization-indepen-

dent structural color based on a coding metasurface via a bidirectional artificial neural network. *J Opt Soc Am B* **41**, 2220–2227 (2024).
46. Yang HL, Ni B, Guo JH et al. Deep learning-enabled inverse design of polarization-selective structural color based on coding metasurface. *Chin Phys B* **34**, 050702 (2025).
47. Wei ZY, Xu WJ, Dong SY et al. Ultraprecision, high-capacity, and wide-gamut structural colors enabled by a mixture probability sampling network. *Light Sci Appl* **15**, 164 (2026).
48. Ma YH, Luo Q, Zhang C et al. Deep learning enables multifunctional metasurfaces design with mutual coupling estimation. *IEEE Trans Antennas Propagat* **72**, 8443–8451 (2024).
49. Noh J, Kim J, Rho J. Overcoming information sparsity in metasurfaces for full-color holography via end-to-end design. *Nano Lett* **25**, 11398–11405 (2025).
50. Xiao CY, Liu MQ, Yao K et al. Ultrabroadband and band-selective thermal meta-emitters by machine learning. *Nature* **643**, 80–88 (2025).
51. Dai P, Sun K, Yan XZ et al. Inverse design of structural color: finding multiple solutions *via* conditional generative adversarial networks. *Nanophotonics* **11**, 3057–3069 (2022).
52. Unni R, Yao K, Zheng YB. Deep convolutional mixture density network for inverse design of layered photonic structures. *ACS Photonics* **7**, 2703–2712 (2020).
53. Li X, Chen LW, Li Y et al. Multicolor 3D meta-holography by broadband plasmonic modulation. *Sci Adv* **2**, e1601102 (2016).
54. Zhang F, Pu MB, Gao P et al. Simultaneous full-color printing and holography enabled by centimeter-scale plasmonic metasurfaces. *Adv Sci* **7**, 1903156 (2020).
55. Yu X, Teng ZL, Fan XH et al. IncepHoloRGB: multi-wavelength network model for full-color 3D computer-generated holography. *Opto-Electron Adv* **8**, 250130 (2025).
56. Kang D, Rho J. Structural color from basic principles to emerging applications. *Opto-Electron Adv* **8**, 250051 (2025).
57. Pastrňák J, Roskovcová L. Refraction index measurements on AlN single crystals. *Phys Status Solidi (B)* **14**, K5–K8 (1966).
58. Rodríguez-de Marcos LV, Larruquert JI, Méndez JA et al. Self-consistent optical constants of MgF_2, LaF_3, and CeF_3 films. *Opt Mater Express* **7**, 989–1006 (2017).

Acknowledgements

This work was partly supported by the National Natural Science Foundation of China (No. 11604205). AI tools were used only for grammar checking and formatting assistance of the manuscript during its preparation.

Author contributions

Tao Zhu: Methodology, Software, Investigation, Data curation, Formal analysis, Visualization, Writing – original draft. Ya Gao: Conceptualization, Methodology, Supervision, Writing – review & editing. Xi Chen: Validation, Formal analysis, Writing – review & editing. Xiaojin Chen: Validation, Investigation, Writing – review & editing. Jiao Geng: Conceptualization, Supervision, Project administration, Funding acquisition, Writing – review & editing. Liping Shi: Methodology, Resources, Writing – review & editing. Chenhui Lu: Conceptualization, Supervision, Project administration, Funding acquisition, Writing – review & editing. All authors reviewed and approved the final manuscript.

Competing interests

The authors declare no competing financial interests.

Open Access This article is licensed under a Creative Commons Attribution 4.0 International License, which permits use, sharing, adaptation, distribution and reproduction in any medium or format, as long as you give appropriate credit to the original author(s) and the source, provide a link to the Creative Commons license, and indicate if changes were made. To view a copy of this license, visit http://creativecommons.org/licenses/by/4.0/
©The Author(s) 2026.

Opto-Electronic Journals Group
www.oejournal.org
Scan for Article PDF